Contents lists available at ScienceDirect

Earth and Planetary Science Letters

www.elsevier.com/locate/epsl



Transport properties of Fe-Ni-Si alloys at Earth's core conditions: Insight into the viability of thermal and compositional convection



Youjun Zhang a,*, Mingqiang Hou b,c, Peter Driscoll d, Nilesh P. Salke c,1, Jin Liu c, Eran Greenberg ^{e,2}, Vitali B. Prakapenka ^e, Jung-Fu Lin ^{f,*}

- ^a Institute of Atomic and Molecular Physics, Sichuan University, Chengdu 610065, China
- b Institute of Meteoritics, Department of Earth and Planetary Sciences, University of New Mexico, Albuquerque, NM 87131, USA
- ^c Center for High Pressure Science and Technology Advanced Research, Beijing 100094, China
- ^d Earth and Planets Laboratory, Carnegie Institution for Science, 5241 Broad Branch Road N.W., Washington, DC 20015, USA
- e Center for Advanced Radiation Sources, University of Chicago, IL 60637, USA
- f Department of Geological Sciences, Jackson School of Geosciences, The University of Texas at Austin, Austin, TX 78712, USA

ARTICLE INFO

Article history: Received 11 June 2020 Received in revised form 24 September 2020

Accepted 26 September 2020 Available online 13 October 2020

Editor: J. Badro

Keywords: Fe alloys high pressure-temperature experiments electrical resistivity thermal conductivity Earth's core geodynamo

ABSTRACT

Thermal and compositional convection in Earth's core are thought to be the main power sources driving geodynamo. The viability and strength of thermally and compositionally-driven convection over Earth's history depend on the adiabatic heat flow across the core-mantle boundary (CMB) which is governed by the thermal conductivity of a constituent Fe-Ni-light element alloy at the pressure-temperature (P-T) conditions relevant to the core. Silicon is often proposed to be an abundant light element alloyed with Fe along with ∼5 wt% Ni, but the thermal transport properties of Fe-Ni-Si alloys at high *P-T* remain largely uncertain. Here we measured the electrical resistivities of Fe-10wt%Ni and Fe-1.8wt%Si alloys up to \sim 142 GPa and \sim 3400 K using four-probe van der Pauw method in laser-heated diamond anvil cell experiments. Our results show that the resistivities of hcp-Fe-1.8Si and Fe-10Ni display quasi-linear temperature dependence from \sim 1500 to 3400 K at each given high pressure. Addition of \sim 2 wt% Si in hcp-Fe significantly increases its resistivity by \sim 25% at \sim 138 GPa and 4000 K, but Fe-10wt%Ni has similar resistivity to pure hcp-Fe at near CMB P-T conditions. Using our measured values of electrical resistivities, we model thermal conductivities via the Wiedemann-Franz law, giving a nominal thermal conductivity of \sim 50 W m⁻¹ K⁻¹ for liquid Fe-5Ni-8Si alloy at the topmost outer core, implying an adiabatic (conductive) core heat flow of \sim 8.0 TW. The outer core has a much lower thermal conductivity than the inner core due to light-element differentiation across the solidifying inner-core boundary. Our studies imply that the adiabatic core heat flow is low enough to enable thermal convection to drive the geodynamo over most and possibly all of Earth's history, while the strength of compositional convection increases with the inner-core growth and accounts for \sim 83% of the buoyancy flux to the present-day geodynamo.

© 2020 Elsevier B.V. All rights reserved.

1. Introduction

Earth's core continuously loses heat to the lower mantle, secularly cooling the core and potentially driving thermally-driven convection to power the geodynamo (Nimmo, 2015). When the liquid core cooled below the melting temperature of the constituent core alloy, the inner core began to solidify. Paleomagnetic records indicate that Earth's magnetic field has existed for at least \sim 3.45 billion years (Tarduno et al., 2010), which has been maintained by the geodynamo through rigorous convective motions in the liquid outer core (Nimmo, 2015). Geodynamo theory is widely accepted for the generation of the magnetic field, but there's much less agreement on the nature of the energy sources that power the geodynamo over the history of Earth (Driscoll and Du, 2019). Typically, thermal and compositional convection are considered to be the main energy sources. A core cooling rate in excess of the conductive (adiabatic) heat flow will produce thermal buoyancy, driving thermal convection in the fluid core, while inner-core solidification releases excess light elements to the outer core that are buoyant compared to the background liquid, driving compo-

^{*} Corresponding authors.

E-mail addresses: zhangyoujun@scu.edu.cn (Y. Zhang), afu@jsg.utexas.edu (J.-F. Lin).

¹ Current affiliation: Department of Physics, University of Illinois at Chicago, Chicago, IL 60607, USA.

² Current affiliation: Applied Physics Department, Soreq Nuclear Research Center (NRC), Yavne 81800, Israel.

Table 1 Thermodynamic parameters used in this study.

Parameters	Symbol	Value used
Inner core radius	r _{icb}	1221 km
Core mantle radius	r_{cmb}	3480 km
Inner-core boundary temperature	T_{icb}	5500 K
Core-mantle boundary temperature	T_{cmb}	4000 K
Temperature gradient at the lowermost mantle	ΔT	1300 K
Density at the topmost outer core	ho	9.90 kg m ⁻³ (Dziewonski and Anderson, 1981)
CMB heat flow	Q_{cmb}	10.0 TW
Adiabatic CMB heat flow	Q_{acmb}	8.0 TW (This study)
Adiabatic ICB heat flow	Q_{aicb}	1.5 TW (This study)
Grüneisen parameter in the core	γ	1.5 (Labrosse, 2015)
Temperature gradient at the topmost outer core	dT_a/dr	1.0 K km ⁻¹ (Labrosse, 2015)
Gravity at CMB	g_{cmb}	10.6823 m s ⁻² (Dziewonski and Anderson, 1981)
Gravity at ICB	G_{icb}	4.4002 m s ⁻² (Dziewonski and Anderson, 1981)
Thermal conductivity at the lowermost mantle	k_{mantle}	10 W m ⁻¹ K ⁻¹ (e.g., Ammann et al., 2014; Hsieh et al., 2018)
Thermal conductivity at the topmost inner core	k_{icb}	138 W m ^{-1} K ^{-1} (This study)
Thermal conductivity at the topmost outer core	K_{cmb}	$50 \text{ W m}^{-1} \text{ K}^{-1}$ (This study)
Heat capacity in the core	C_p	$650 \mathrm{Jkg^{-1}K^{-1}}$
Thermal expansivity in the core	$\alpha^{'}$	$1.53 \times 10^{-5} \text{ K}^{-1}$

sitional convection (Driscoll and Du, 2019). Besides, other energy sources have also been proposed, such as the exsolution of light constitution (e.g., magnesium) before the inner core formation or tidally driven flows (Badro et al., 2016; O'Rourke and Stevenson, 2016). However, the relatively large uncertainty of the thermodynamic state of the core makes it difficult to estimate the relative contributions of these various mechanisms (Driscoll and Du, 2019). Regardless of the specific energy source, the thermal conductivity of the core that is fundamental to understanding the energetic state of the core remains uncertain.

The heat flow out of the core into the mantle (core-mantle boundary heat flow, Q_{cmb}) is controlled by the thermal conductivity of the lower mantle and the temperature gradient in the lowermost mantle, while the adiabatic (conductive) core heat flow (Q_{acmb}) is controlled by the thermal conductivity of the constituent liquid Fe-Ni and its alloys with candidate light elements (Nimmo, 2015). Higher thermal conductivity of the core would lead to larger adiabatic heat flux and make thermal convection more difficult. According to Schwarzschild's criterion, thermal convection only happens when the Q_{cmb} is greater than the Q_{acmb} (Schatten and Sofia, 1981). The present-day Q_{cmb} is estimated to be \sim 10 TW based on the thermal conductivity of the Earth's lowermost mantle materials (\sim 10 W m⁻¹ K⁻¹) (e.g., Ammann et al., 2014; Hsieh et al., 2018) and a temperature drop of \sim 1300 K across the lowermost \sim 190 km of the mantle (see Table 1 and details in Supplementary Material Note-2). For years Qacmb was estimated to be around 3-5 TW according to a modeled thermal conductivity of the core (\sim 30 W m⁻¹ K⁻¹) (Stacey and Loper, 2007). Consequently, thermal convection was commonly assumed to maintain the geodynamo back in deep time. Recent upward revisions of the thermal conductivity of the core to 130-200 $\mathrm{W}\,\mathrm{m}^{-1}\,\mathrm{K}^{-1}$ indicate a larger adiabatic heat flow of 13–16 TW and larger values of Q_{cmb} to avoid a deep stratified layer. Larger values of Q_{cmb} lead to younger inner core nucleation ages of ~ 0.7 Ga (Ohta et al., 2016; Pozzo et al., 2012). However, higher thermal conductivity may also imply thermal stratification prior to inner core nucleation. This raises the "core paradox" that the geodynamo did not have an energy source before inner core formation but paleomagnetic evidence indicates the magnetic field is much older than the inner core (Olson, 2013). To address this debate and reduce uncertainty in the energetic state of the core, the thermal conductivity of liquid iron alloys at Earth's core conditions needs to be precisely determined.

There are two common ways to obtain the thermal conductivity of Fe and Fe alloys at the pressure-temperature (P-T) conditions of the core. One is to measure their electrical resistivity using an elec-

trode method at high P-T (e.g., Inoue et al., 2020; Ohta et al., 2016; Zhang et al., 2020). The measured electrical conductivity may be converted to thermal conductivity through the Wiedemann-Franz law which assumes that both electrical and thermal transport are dominated by the free electrons in metals. The second way is to model thermal conductivity using a flash transient heating technique (Konôpková et al., 2016) or a time-domain thermoreflectance technique (Hsieh et al., 2018). Several studies have been performed to obtain the electrical and/or thermal conductivities of Fe and Fe alloys at high P-T using laser-heated Diamond Anvil Cells (DACs) and shock-wave compression (e.g., Gomi et al., 2016, 2013; Konôpková et al., 2016; Matassov, 1977; Ohta et al., 2016; Zhang et al., 2020). However, these results were inconsistent: for example, the thermal conductivity of Fe varied by a factor of \sim 7 from ~ 30 to 226 W m⁻¹K⁻¹ at relevant *P-T* conditions of the CMB (Williams, 2018). The discrepancies in experiments might be due to the use of sample geometry (four-probe van der Pauw method vs. pseudo-four probe), sample irregularity, leaser-heating issues, and/or the uncertainty of experimental extrapolation (e.g., Dobson, 2016; Zhang et al., 2020). For example, previous resistivity measurements in laser-heated DAC experiments by Ohta et al. (2016) used pseudo-four probe method (or two-probe electrodes) in which the electrical conductivity measurements can be significantly influenced by sample shape and thickness. In addition, it has been discussed in recent studies that the heterogeneous temperature distribution of the sample in previous laser-heated DAC experiments can contribute to an underestimate of the resistivity of iron at high P-T (Inoue et al., 2020; Zhang et al., 2020).

A recent study applied homogeneous flat-top laser-heating to an hcp-Fe sample with a suitable geometry and measured its electrical resistivity by a four-probe van der Pauw method at the relevant P-T conditions of the core in laser-heated DACs (Zhang et al., 2020). The measured resistivity in hcp-Fe at high P-T agrees with first-principles computations that consider both electron-phonon and electron-electron scattering through first-principles lattice dynamics (FPLD) and density functional perturbation theory (DFPT) (Xu et al., 2018), which is significantly larger than theoretical calculations if electron-electron contribution is neglected (de Koker et al., 2012; Pozzo et al., 2012, 2014). The thermal conductivity of hcp-Fe is determined to be \sim 100 W m $^{-1}$ K $^{-1}$ near CMB conditions (\sim 136 GPa and \sim 4000 K) through the Wiedemann-Franz law in both experiments and theory.

The Earth's core is composed of Fe-Ni alloy with some amount of light element(s), such as Si, S, O, C, and H (Li and Fei, 2014). 5–10 wt% Ni is suggested in the core according to chondritic bulk Earth models (Li and Fei, 2014). As suggested by the partitioning

of light elements between silicates and iron melt and the velocitydensity comparisons between geophysical modeling and seismic studies of the core (e.g., Badro et al., 2015, 2014; Siebert et al., 2012), O and Si are the two leading candidate light elements to be abundantly present in the core. Here we use Si as a representative light element to investigate its effects on electrical and thermal conductivity of iron at high P-T because it is readily soluble in iron at ambient pressure and remains soluble and stable in hcp-Fe structure at the relevant P-T conditions of the inner core (Komabayashi et al., 2019; Lin et al., 2009). High-pressure mineral physics suggests Fe alloyed with approximately 8-10 wt% and 2-5 wt% Si may satisfy the density deficit of the outer and inner core, respectively, assuming that the Earth's core is predominantly an Fe-Si alloy (see Supplementary Material Note-1) (e.g., Fischer et al., 2014; Mao et al., 2012). Therefore, Ni and light element effects on the electrical and thermal conductivity should be quantified to understand the energetics of the core. A recent study measured the electrical resistivities of hcp-Fe-2wt%Si at \sim 44 GPa up to \sim 1400 K, Fe-4wt%Si at \sim 46 and 99 GPa up to \sim 3100 K, and Fe-6.5wt% Si at \sim 99 GPa up to 1900 K in an internally heated DAC (Inoue et al., 2020). This study indicates that the resistivity of Fe-Si alloys may approach saturation at high P-T relevant to the top of the outer core, suggesting that the thermal conductivity of an Fe-Si core may be high enough to induce a rapid growth of the inner core. However, high P-T time-domain thermoreflectance experiments indicate that Si can significantly lower the thermal conductivity of iron (Hsieh et al., 2020), which suggests a low thermal conductivity of the core. Furthermore, the experimental conditions by Inoue et al. (2020) are still lower than the relevant P-T conditions of the topmost outer core and the reported saturation effect is inconsistent with theoretical predictions (Pozzo and Alfè, 2016; Pozzo et al., 2014; Zhang et al., 2020). Therefore, the combined effects of Ni and Si on the transport properties of iron at high P-T remain to be investigated.

In this study, we used a four-probe van der Pauw method in laser-heated DACs to directly measure the electrical resistivity of Fe-10wt%Ni (Fe-10Ni) and Fe-1.8wt%Si (Fe-1.8Si) alloys in the hcp structure from ~ 80 to ~ 140 GPa and up to ~ 3400 K. The experimental results are then used to model the thermal conductivity of the alloys at the relevant P-T conditions of the core using the Wiedemann–Franz law. Our results show that the thermal conductivity of iron is significantly lowered by the light element Si, indicating a lower adiabatic core heat flow than previous estimates. Besides, light element segregation at the inner-core boundary (ICB) can result in a higher thermal conductivity in the inner core, causing a super-adiabatic temperature in the inner core. Our study provides constraints on the strength of thermal and compositional convection to maintain the geodynamo and its evolution over the geological time.

2. Materials and methods

Polycrystalline Fe-10(\pm 0.5)wt%Ni (Fe-10Ni) and Fe-1.8(\pm 0.1) wt%Si (Fe-1.8Si) alloys initially in *bcc* structure were used as the starting materials. Fe-10Ni alloy was the same one used in the previous work (Lin et al., 2002), which was obtained from Dr. William A. Basset at Cornell University. The Fe-1.8Si alloy was obtained from Dr. Leonid Dubrovinsky at the University of Bayreuth, which was synthesized from a mixture of powder iron and silicon with a starting atomic ratio of 96.4:3.6. Fe-10Ni and Fe-1.8Si alloys were compressed to thin foil with an initial thickness of less than \sim 2(0.3) µm. They then were shaped into a uniform Greek cross shape with a diameter of \sim 6 µm at the center using a Focused Ion Beam (FIB: FEI Versa 3D) at the Center for High Pressure Science and Technology Advanced Research (HPSTAR). Diamond anvils with 100-300 µm beveled culets with a beveled angle of 9 de-

grees were used to generate high pressures in diamond anvil cells (DACs). The sample was loaded into the sample chamber of the DACs and sandwiched between two dried SiO₂ layers as shown in Fig. 1a. The loaded samples were compressed to targeted pressures and were subsequently heated using a flat-top double-sided laser heating system as Figs. 1a and 1b show. The complete experimental details were previously discussed in the literature (Zhang et al., 2020).

Analyses of the quenched samples after high P-T experiments using Scanning Electron Microscopy/Energy Dispersive X-Ray Spectroscopy (SEM/EDS) in FIB (FEI Verse 3D) showed a chemical composition of Fe with 1.85(10) wt% Si for Fe-1.8Si and Fe with 9.84(0.52) wt% Ni for Fe-10Ni alloy (Figs. 1c and 1d; Tables S1 and S2). These analyses show that the samples were chemically homogeneous without observable chemical contaminations within analytical uncertainties (Supplementary Material Tables S1 and S2). The recovered Fe-1.8Si and Fe-10Ni alloys were \sim 1.5 μ m and \sim 1.3 μ m in thickness (Figs. 1c and 1d), respectively.

Resistivity measurements of Fe-10Ni and Fe-1.8Si alloys were performed at high pressures from ~80 to ~140 GPa and high temperatures up to \sim 3400 K at the 13-IDD beamline station at the GeoSoilEnviroConsortium for Advanced Radiation Sources (GSE-CARS) of the Advanced Photon Source (APS). We measured the electrical resistivity of Fe-10Ni and Fe-1.8Si alloys by a van der Pauw method using a Multimeter source (Keithley 6221 model) and an ultra-low voltmeter (Keithley 2182A model) during laser heating in Fig. 1b. A constant direct current of 5-10 mA was applied in the resistivity measurements. The voltage was measured between probes C and D and between A and D when the direct current passed through the sample from leads A to B and from B to C, respectively. An average value of measured voltages was used to obtain the resistance (R). The resistivity at high temperatures was obtained using $\rho = \rho_0 (R/R_0) (V/V_0)^{1/3}$ (Gomi et al., 2013), where R_0 and V_0 are the resistance and volume at high pressure and room temperature, respectively, and V is the measured volume by in situ X-ray diffraction (XRD) at high pressuretemperature. In situ synchrotron XRD patterns were collected by a Pilatus 1M CdTe detector before, during, and after the laser heating, respectively, at GSECARS. Thermal radiation spectra from the heated areas were collected to determine the temperatures of the samples. Care was taken to ensure that the Greek cross shape area was heated homogeneously; the temperature variation across the region was typically within 5% of the measured temperatures.

The experimental P-T conditions in the electrical resistivity measurements for Fe-1.8Si and Fe-10Ni alloys are shown in Fig. S2 in the Supplementary Material. Only hcp structure in both Fe-10Ni and Fe-1.8Si was observed over the investigated P-T range, consistent with previous works (Komabayashi et al., 2019; Lin et al., 2002), as examples in Figs. S3 (Fe-10Ni) and S4 (Fe-1.8Si). The pressure was determined from the measured lattice parameter of hcp-Fe-10Ni and hcp-Fe-1.8Si by in situ XRD and their thermal equation of state (Asanuma et al., 2011; Lin et al., 2002). Thermal pressures in the experiments are modeled from the thermal equation of states of hcp-Fe and Fe alloys (Fei et al., 2016). Collected XRD patterns show evenly distributed intensity in the caked diffraction lines in both hcp-Fe-10Ni and hcp-Fe-1.8Si over our investigated P-T range in Figs. S3 and S4, indicating that the sample had no significant texture due to compression or crystal growth at high temperatures in the experiments.

3. Results

3.1. Electrical resistivity of Fe-1.8Si alloy at high pressures

Electrical resistivities of polycrystalline Fe-1.8Si alloy were measured up to \sim 138 GPa at room temperature upon compression and

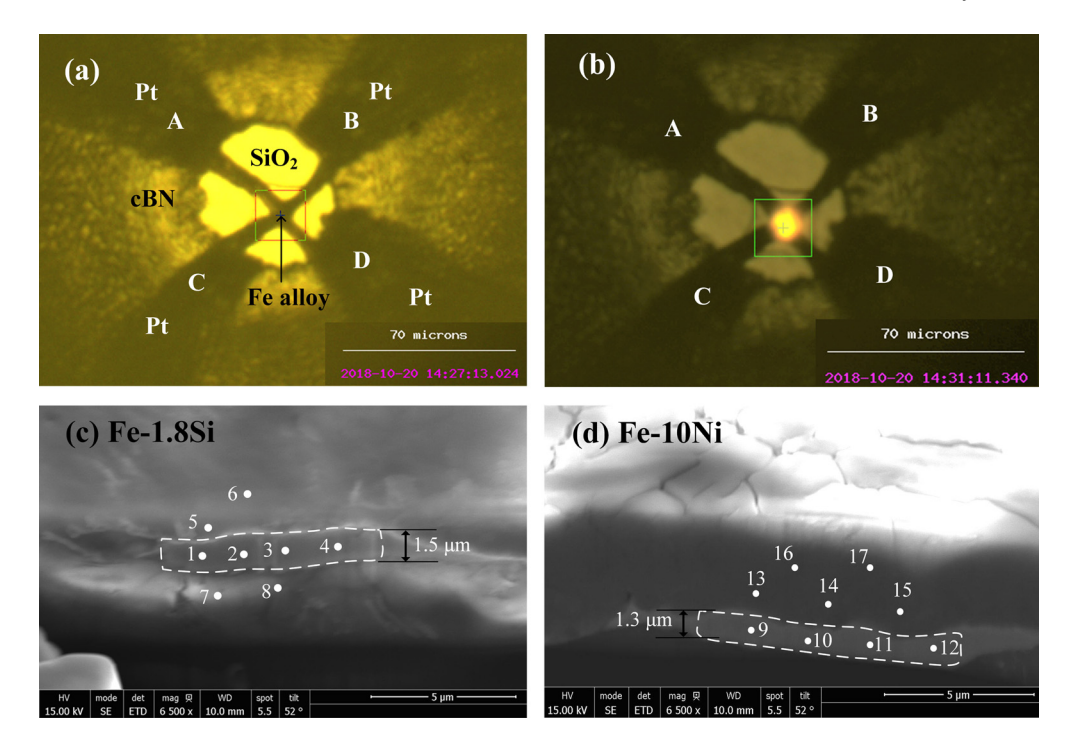


Fig. 1. Electrical resistivity measurements of Fe alloys in a laser-heated DAC and SEM microphotographs of recovered samples. (a) Representative image of an experimental assembly for the electrical resistivity measurements using the four-probe van der Pauw method in a LHDAC. The image shows an Fe-1.8Si alloy loaded in a sample chamber with cBN gasket insert, SiO₂ insulator, and four Pt leads at \sim 138 GPa and 300 K. (b) The cross heart area of Fe-1.8Si alloy was double-side heated to \sim 1978 K at \sim 138 GPa by continuous laser-heating with a laser spot size of \sim 10 µm in diameter on both sides of the sample. Analysis of the measured thermal radiation spectra shows homogenous temperature distributions on both sides of the sample. (c) Recovered Fe-1.8Si alloy sample with a thickness of around 1.5 µm at ambient pressure (white dashed-line) after FIB cutting. (d) Recovered Fe-10Ni alloy sample with a thickness of around 1.3 µm at ambient pressure (white dashed line). The white dots in (c) (points 1-8) and (d) (points 9-17) show the locations of the SEM/EDS analyses of the samples and surrounding thermal insulator (silica). The analysis results are listed in Supplementary Material Tables S1 and S2.

decompression, respectively (Fig. S1 in the Supporting Material). With increasing pressure up to \sim 12 GPa, the resistivity decreases in bcc-Fe-1.8Si. A bcc to hcp phase transition happens in Fe-1.8Si at between \sim 12 and \sim 17 GPa with a resistivity jump, similar to that in pure iron (Gomi et al., 2013). The resistivity increases from ~ 16.7 to $\sim 30.0~\mu\Omega$ cm with the phase transition. With further increasing pressure above \sim 17 GPa, the resistivity gradually diminishes. After high pressure-temperature experiments, we decompressed the sample and measured its resistivity as well. The measured resistivities upon compression and decompression do not deviate from each other. The hcp returns to bcc phase happening at around 8 GPa on decompression, where it shows a maximum resistivity of \sim 36.0 $\mu\Omega$ cm. Our pressure-dependent resistivity is consistent with previous measurements in Fe-Si systems (Gomi et al., 2016), where the resistivity of Fe-1.8Si is generally located between the Fe-1Si and Fe-2Si at high pressures. The pressure-dependent resistivity in hcp-Fe-1.8Si becomes flattened at high pressures above \sim 80 GPa, showing that the pressure effect on the resistivity is getting weaker with increasing pressure.

3.2. Electrical resistivity of Fe-1.8Si alloy at high P-T

Electrical resistivities of hcp-Fe-1.8Si were measured up to \sim 3400 K at 88(3), 106(3), 120(4), and 138(4) GPa in double-sided laser-heated DACs along with in situ XRD measurements. XRD showed the sample being in hcp structure in the investigated P-T range as shown in Fig. S3 in the Supplementary Material. The measurements at these given pressure points show that the resistivity of Fe-1.8Si increased quasi-linearly with increasing temperature up to 3400 K (red solid circles, Fig. 2). Temperature dependence of the resistivity in hcp-Fe-1.8Si can be given by the Bloch-Grüneisen formula above the Debye temperature (θ_D) with a residual resistivity (ρ_0):

$$\rho_{\text{Fe-1.8Si}}(V,T) = \rho_0 + \rho_{BG}(V,T)$$

$$= \rho_0 + D(V) \left(\frac{T}{\theta_D(V)}\right)^n$$

$$\times \int_0^{\theta_D(V)/T} \left[\frac{z^n}{(e^z - 1)(1 - e^{-z})}\right] dz \tag{1}$$

where ρ_0 is a constant value when the temperature (T) of the metal or alloy is sufficiently reduced so that all the phonons are frozen. Fitting the measured resistivities at high P-T simultaneously yielded ρ_0 , n, and D(V) constants. In the case of pure Fe, ρ_0 is assumed to be 0 Ω m for simplicity as the true residual value at close to 0 K is much smaller than that at high P-T conditions. We should also note that the ρ_0 depends not only on the metal but also on its impurity concentration. The fitted parameters for the Bloch-Grüneisen formula in hcp-Fe-1.8Si alloy at high P-T are shown in Table 2. The fitted residual resistivity ρ_0 in hcp-Fe-1.8Si is between ${\sim}6$ and ${\sim}12~\mu\Omega\,cm$ at 88-138 GPa and near 0 K. The temperature response in resistivity of hcp-Fe-1.8Si becomes weaker with increasing pressure from 88 to 138 GPa as the parameters "n" and "D(V)" are reduced upon compression. The temperature-dependent resistivity in hcp-1.8Si alloy does not show significant resistivity saturation up to 3400 K at high pressures. Our experiments were limited to ~3400 K because of the fast recrystallization and degradation of the sample. As such, theoretically predicted non-linear behavior of iron or iron alloy at temperatures above \sim 4000 K (Pozzo and Alfè, 2016) will need to be further tested in the future.

The resistivity of Fe-2Si alloy was recently measured at \sim 44 GPa and up to \sim 1400 K in a resistance-heated DAC (black squares, Fig. 2a) (Inoue et al., 2020). Even though the temperature response of the resistivity in *hcp*-Fe-2Si is similar to our results in Fe-1.8Si

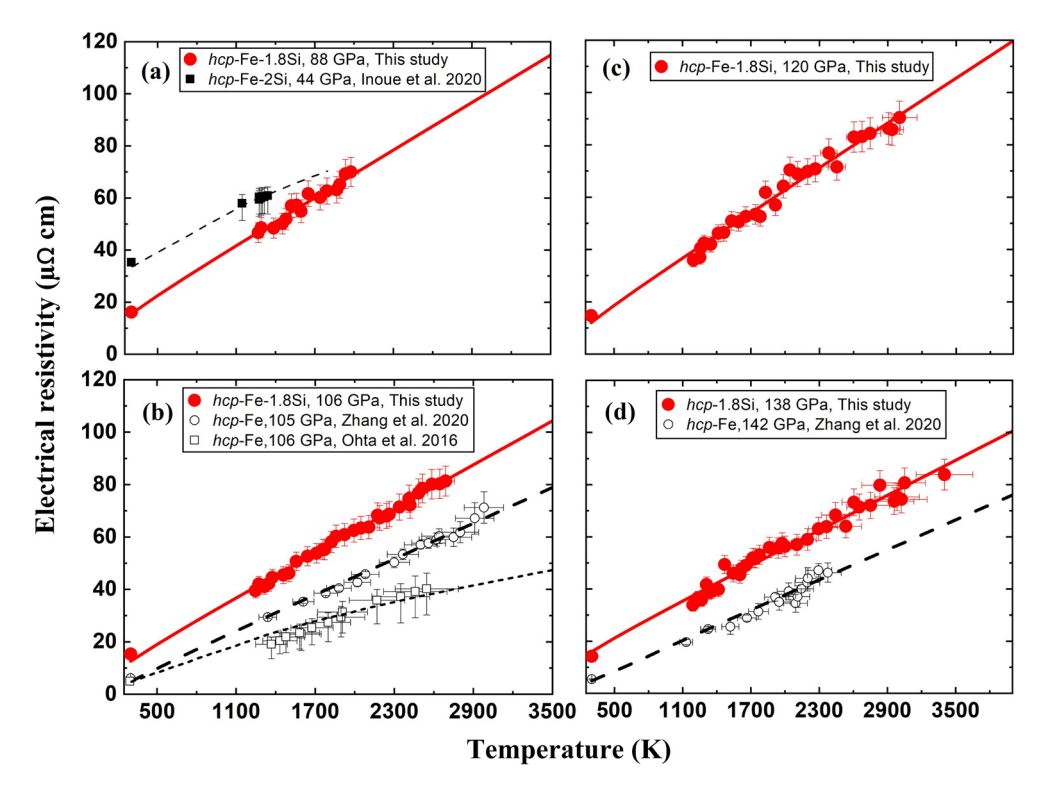


Fig. 2. Temperature-dependent electrical resistivity of *hcp*-Fe-1.8Si alloy at high pressures. Electrical resistivity of the Fe-1.8Si alloy was measured up to: (a) 1976(40) K at 88(3) GPa; (b) 2690(67) K at 106(3) GPa; (c) 3005(152) K at 120(4) GPa; and (d) 3402(250) K at 138(4) GPa. Within experimental uncertainties, the measured resistivities quasi-linearly increase with increasing temperature (red circles with crosses) and can be well modeled using the Bloch-Grüneisen formula (red lines). Previous experimental results of *hcp*-Fe at 105 GPa and 142 GPa (open circles and dashed lines) by Zhang et al. (2020) and at 106 GPa (open squares and short-dash line) by Ohta et al. (2016), respectively, are also plotted for comparisons. The resistivities of *hcp*-Fe-2Si at ~44 GPa and up to ~1400 K by Inoue et al. (2020) (closed black squares) are also compared. (For interpretation of the colors in the figure(s), the reader is referred to the web version of this article.)

Table 2 Parameters for the Bloch-Grüneisen formula in the resistivity of *hcp*-Fe-1.8Si alloy at high *P-T*.

Pressure (GPa)	θ _D (K)	$ ρ_0 $ (μ $Ω$ cm)	D(V)	n
88(3)	630	9.2(1.8)	19.07(0.72)	0.74(0.03)
106(3)	656	6.9(0.8)	18.32(0.27)	0.67(0.03)
120(4)	675	6.3(1.6)	19.19(0.56)	0.65(0.05)
138(4)	698	11.6(1.4)	15.55(0.46)	0.63(0.05)

Debye temperature (θ_D) was assumed to the same with hcp-Fe (Dewaele et al., 2006).

at 88 GPa, our data at higher temperatures do not show the "resistivity saturation" that was inferred for *hcp*-Fe-2Si in Inoue et al. (2020) using limited *P-T* data. It is likely that the four-probe van der Pauw method with a homogeneously heated sample helped reduce the sample shape, thickness, and temperature variation effects in electrical conductivity measurements. On the other hand, the resistivity saturation reported by Ohta et al. (2016) and Inoue et al. (2020) using the pseudo four-probe method could be an artifact of the aforementioned factors.

We compared the measured temperature-dependent resistivity in hcp-Fe-1.8Si with that of hcp-Fe at similar pressures of \sim 106 GPa and \sim 138 GPa by Ohta et al. (2016) and Zhang et al. (2020) in Figs. 2b and 2d, respectively. As discussed above, the results by Ohta et al. (2016) likely underestimated the resistivity of hcp-Fe at high P-T because of the experimental issues (e.g., temperature distribution and uncontrolled sample geometry) (Fig. 2b). Here we have mainly compared our results with that of iron reported by Zhang et al. (2020) because both studies had used the same experimental methods and the quasi-linear resistivity results by Zhang et al. (2020) are confirmed by most recent first-principles calcula-

tions that considered both electron-electron and electron-phonon scattering effects at high P-T (Xu et al., 2018). These results show that adding 1.8 wt% Si into hcp-Fe can significantly increase its resistivity up to 3400 K at high pressures. When we apply the Bloch-Grüneisen formula to extrapolate the measured resistivity to higher temperatures, the resistivity in hcp-Fe-1.8Si is around 100 $\mu\Omega$ cm at the relevant conditions of the topmost outer core ($\sim\!138$ GPa and 4000 K), which is approximately 25% higher than that in hcp-Fe ($\sim\!80~\mu\Omega$ cm) (Fig. 2d).

3.3. Electrical resistivity of Fe-10Ni alloy at high P-T

Similar experiments on electrical resistivity and *in situ* XRD measurements in the hcp-Fe-10Ni alloy were conducted up to \sim 3000 K at high pressures from \sim 86 to 143 GPa (Fig. S4 in the Supplementary Material). The results show three main features at varied temperatures (Fig. 3): (1) the minimum resistivity at low temperatures (below \sim 1500 K) due to resonant impurity scattering (ρ^{imp}); (2) the residual resistivity (ρ_0); (3) the quasi-linear slope of the resistivity (ρ_{BG}) at moderate temperatures above approximate 1500 K due to electron-phonon scattering (Boekelheide et al., 2009). We use the following formula to describe these features in the measured resistivity of hcp-Fe-10Ni alloy as a function of temperature:

$$\rho_{\text{Fe-10Ni}}(V,T) = \rho^{\text{imp}}(T) + \rho_0 + \rho_{BG}(V,T)$$
 (2)

The temperature-dependent resonant impurity term can be taken from the following form (Volkov, 1984):

$$\rho^{imp}(T) = \frac{\rho_0^{imp}}{1 + \left(T/\theta_{imp}\right)^2} \tag{3}$$

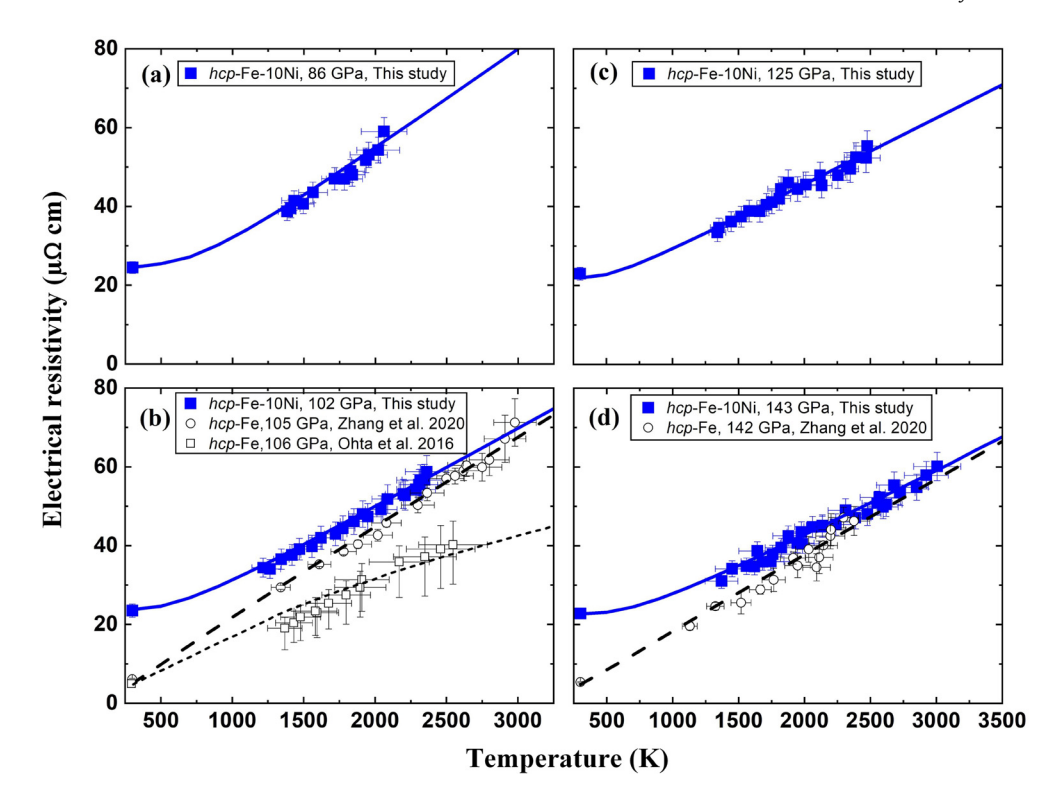


Fig. 3. Temperature-dependent electrical resistivity of *hcp*-Fe-10Ni alloy at high pressures. Electrical resistivity of the Fe-10Ni alloy was measured up to: (a) 2060(150) K at 86(2) GPa; (b) 2362(140) K at 102(2) GPa; (c) 2476(100) K at 125(3) GPa; and (d) 3006 (178) K at 143(3) GPa. The measured resistivities within uncertainties (blue squares with crosses) increase almost quasi-linearly with increasing temperature at above 1500 K and are close to that of pure iron at high *P-T*. Blue curves are fitted using Bloch-Grüneisen formula and temperature-dependent resonant impurity resistivity. Previous experimental results of *hcp*-Fe at 105 GPa and 142 GPa (open black circles and black dashed lines) by Zhang et al. (2020) and at 106 GPa (open squares and short-dash line) by Ohta et al. (2016), respectively, are also plotted for comparisons.

Table 3 Parameters for the Bloch-Grüneisen formula in the resistivity of *hcp*-Fe-10Ni alloy at high *P-T*.

Pressure (GPa)	θ_D (K)	$ ρ_0 $ (μ $Ω$ cm)	D(V)	п	$ ho_0^{imp} \ (\mu\Omega{ m cm})$	$ heta_{imp}$ (K)
86(3)	627	3.26(2.03)	15.97(0.76)	1.07(0.07)	24.5(4.4)	452(80)
102(3)	650	9.70(0.84)	13.00(0.28)	0.74(0.17)	15.1(3.1)	420(60)
125(4)	681	11.94(1.04)	11.49(0.37)	0.43(0.27)	12.5(1.5)	318(90)
143(4)	704	9.24(0.97)	11.67(0.32)	0.68(0.14)	14.2(1.3)	526(50)

Debye temperature (θ_D) was assumed to the same with $hcp ext{-Fe}$ (Dewaele et al., 2006).

where ρ_0^{imp} is the maximum of the resonant impurity scattering and θ_{imp} is a parameter related to the energy width of the localized states leading to resonant impurity scattering and the energy difference between these states and the Fermi energy. This impurity resistivity varies as T^{-2} , increasing as the temperature decreases. Therefore, the total resistivity of hcp-Fe-10Ni could be written as a sum of multiple terms:

$$\rho_{\text{FeNi}}(V,T) = \frac{\rho_0^{imp}}{1 + \left(T/\theta_{imp}\right)^2} + \rho_0 + D(V) \left(\frac{T}{\theta_D(V)}\right)^n$$

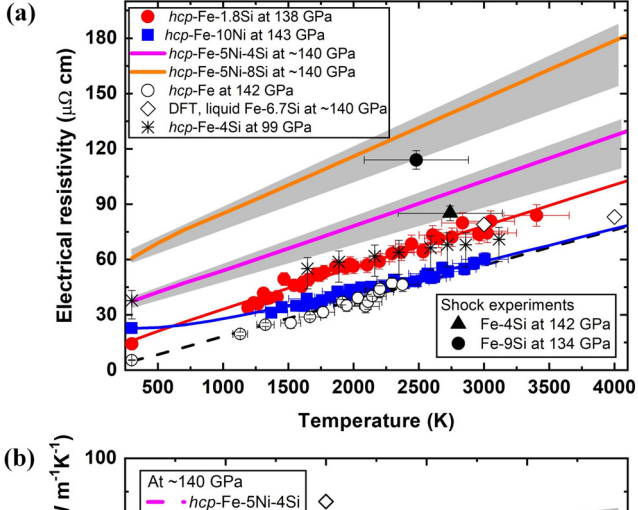
$$\times \int_0^{\theta_D(V)/T} \left[\frac{z^n}{(e^z - 1)(1 - e^{-z})}\right] dz \tag{4}$$

The measured resistivity in hcp-Fe-10Ni was fitted by a least-squares equation at each given pressure point (blue curves in Fig. 3 and Table 3). The modeled resistivity of Fe-10Ni shows non-linear relation between resistivity and temperature from room temperature to \sim 1500 K, and quasi-linear relation between \sim 1500 K and \sim 3000 K, indicating a strong resonant impurity scattering in Fe-10Ni alloy. In comparison, the hcp-Fe-1.8Si does not significantly show the impurity scattering resistivity, which is possibly because

the Si concentration is still small. The measured resistivity of hcp-Fe-10Ni is higher than that of hcp-Fe at room temperature (Ohta et al., 2016; Zhang et al., 2020) (Figs. 3b and 3d). With increasing temperature, the resistivities in hcp-Fe-10Ni and hcp-Fe by Zhang et al. (2020) become close to each other because the ρ^{imp} in hcp-Fe-10Ni is depressed by high temperatures. Therefore, adding 10wt% Ni into iron only has a minor effect on its resistivity when considering the measurement uncertainty at near CMB P-T conditions (\sim 143 GPa and \sim 4000 K).

3.4. Electrical resistivity and thermal conductivity of the core constituent

We modeled the resistivity of Fe-5wt%Ni-8wt%Si (Fe-5Ni-8Si) as a candidate outer-core composition and Fe-5wt%Ni-4wt%Si (Fe-5Ni-4Si) as a candidate inner-core composition (*e.g.*, Fischer et al., 2014; Mao et al., 2012; Zhang et al., 2018) at the relevant *P-T* conditions of the core based on the measured resistivities of *hcp*-Fe-10Ni and *hcp*-Fe-1.8Si alloys. For simplicity, we consider that the Fe-5Ni-4Si and Fe-5Ni-8Si remain in the *hcp* phase, although for a Si-rich Fe alloy (such as Fe-8Si alloy), it may undergo a phase transition from *hcp* to *bcc* (or a mixture of *hcp* and *bcc* phases) at high *P-T* conditions (Fischer et al., 2014). The electrical resistiv-



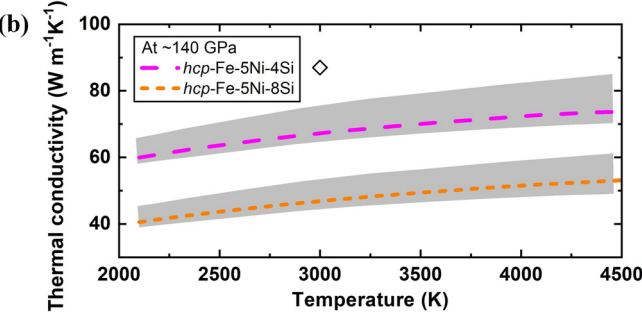


Fig. 4. Electrical resistivity and thermal conductivity of Fe alloys at the relevant P-T conditions of the topmost outer core. (a) Experimentally measured resistivities of hcp-Fe and hcp-Fe alloys. Matthiessen's rule is used to model resistivities of hcp-Fe-5Ni-4Si (solid magenta curve with gray uncertainty region) and hcp-Fe-5Ni-8Si (solid orange curve with gray uncertainty region) at \sim 140 GPa and high temperatures. Experimental results of Fe-4Si at $\sim\!$ 142 GPa (solid black triangles) and Fe-9Si at ~134 GPa (solid black circles) under shock loading (Matassov, 1977) and theoretical calculation of liquid Fe-6.7Si (open diamonds) by DFT (de Koker et al., 2012) are also plotted for comparisons. Recent resistivity results of hcp-Fe-4Si at 99 GPa and up to \sim 3100 K (black asterisks) (Inoue et al., 2020) are lower than the modeled resistivities of hcp-Fe-5Ni-4Si. (b) Thermal conductivity of hcp-Fe-5Ni-4Si (magenta dashed-line with gray uncertainty region) and Fe-5Ni-8Si (orange short dashed-line with gray uncertainty region) at ~140 GPa and high temperatures. Wiedemann-Franz law is used to convert electrical conductivities of Fe-Ni-Si alloys to thermal conductivities using Lorenz number calculated by de Koker et al. (2012). Our modeled thermal conductivity of Fe-Ni-Si alloy is lower than the theoretical calculation of liquid Fe-6.7Si (open diamonds) at the similar P-T conditions (de Koker et al.,

ity arising from independent scattering terms is additive using the Matthiessen's rule:

$$\rho_{hcp\text{-Fe alloy}} = \rho_{hcp\text{-Fe}} + \sum_{n} \rho_{i,n} \cdot x_n \tag{5}$$

where $\rho_{hcp\text{-Fe alloy}}$, $\rho_{hcp\text{-Fe}}$, $\rho_{i,n}$, and x_n are the resistivities of hcp-Fealloy, hcp-Fe, the alloying resistivity of element n for one percent, and the atomic concentration of element n in hcp-Fe, respectively. The modeled resistivities of hcp-Fe-5Ni-4Si (blue line) and hcp-Fe-5Ni-8Si (orange line) at \sim 140 GPa are shown as a function of temperature and compared with previous experiments by shock compression (Matassov, 1977) and first-principles calculations (de Koker et al., 2012) in Fig. 4a. Our model adopts the quasi-linear temperature-dependent resistivity and the linear impurity effects, and provides the upper bounds of the resistivity of Fe-Ni-Si alloy at the relevant P-T conditions of the topmost outer core. However, a saturation effect on high-temperature resistivity of hcp-iron above ~4000 K has been reported in recent theoretical calculations (Pozzo and Alfè, 2016). Additionally, in the Fe-Si system, the Matthiessen's rule could be violated at higher Si contents up to \sim 9 wt% due to the collapse of the large portion of the Fermi surface (Gomi et al., 2016). These could then lead to thermal conductivity increase with depth higher than that predicted by our model

Our modeled resistivities of hcp-Fe-5Ni-4Si and hcp-Fe-5Ni-8Si are generally consistent with the measured resistivities of Fe-4Si and Fe-9Si alloys within uncertainty, respectively, at the similar P-T conditions by shock-wave experiments (Matassov, 1977). However, the modeled resistivities of hcp-Fe-5Ni-4Si are higher than the recently measured hcp-Fe-4Si (at \sim 99 GPa and up to \sim 1900 K) (black asterisks, Fig. 4a) (Inoue et al., 2020). Our experimental data constrain the electrical resistivity of hcp-Fe-5Ni-4Si and hcp-Fe-5Ni-8Si to be $\sim 126^{+5}_{-17}$ $\mu\Omega$ cm and $\sim 177^{+5}_{-25}$ $\mu\Omega$ cm at \sim 4000 K and \sim 140 GPa, respectively, close to the CMB conditions (Komabayashi et al., 2019; Zhang et al., 2018). Since the outer core is liquid, a \sim 7-10% resistivity increase upon melting in Fe or Fe-Si alloy has been suggested (Silber et al., 2019; Xu et al., 2018) and is also considered for the electrical resistivity of liquid Fe-5Ni-4Si and Fe-5Ni-8Si at outer core P-T conditions.

We have also applied the Wiedemann-Franz law to convert the electrical resistivity (ρ) to thermal conductivity ($\kappa = LT/\rho$, L is Lorenz number). At the top of the outer core conditions, the Lorenz number is reported to be ${\sim}2.2\text{--}2.3{\times}10^{-8}~\text{W}\Omega\,\text{K}^{-2}$ in liquid Fe-Si alloy by first-principle calculations (de Koker et al., 2012). If we use the calculated Lorenz number for the Fe-Ni-Si alloys, the temperature-dependent thermal conductivity can be obtained at \sim 140 GPa in Fig. 4b, which generally increase 20–30% with increasing temperature from 2000 to 4500 K. Consequently, the thermal conductivities of hcp-Fe-5Ni-4Si and hcp-Fe-5Ni-8Si are estimated to be 73^{+11}_{-3} and 52^{+8}_{-2} W m⁻¹K⁻¹ at the relevant conditions of the CMB, respectively. The thermal conductivity of liquid Fe-5Ni-8Si can be then constrained to be ${\sim}50~\text{W}\,\text{m}^{-1}\,\text{K}^{-1}$ at the top of the outer core. Our determined thermal conductivity of an Fe-Ni-Si core lies between the estimates of high (90-130 W m⁻¹ K⁻¹) (de Koker et al., 2012; Ohta et al., 2016; Pozzo et al., 2012, 2014) and low $(18-30 \text{ W m}^{-1} \text{ K}^{-1})$ (Hsieh et al., 2020; Konôpková et al., 2016; Stacey and Loper, 2007) values. As discussed in the introduction, the core may also contain other light elements such as O and S, so the thermal conductivity of the core would certainly depend on the exact identities and amounts of these elements. As an example, the thermal conductivity of Fe-O alloy could be drastically different from Fe-Si alloy system because O likely substitutes for the interstitial sites of iron, instead of Si replacing hcp-Fe lattice positions (Williams, 2018). The effects of O on the thermal conductivity of Fe and Fe-Ni-Si alloy in the core need to be investigated by future high P-T experiments in order to address these open questions.

4. Discussion

4.1. Adiabatic heat conduction out of the core

Heat conduction from the Earth's core to the lower mantle over time leads to the secular cooling of the molten Fe core, causing liquid Fe alloy to crystallize to form a solid inner core. According to our preferred thermal conductivity value of $\sim\!50~\rm W\,m^{-1}\,K^{-1}$ for an Fe-5Ni-8Si liquid alloy at the top of the outer core (κ_{toc}) , the adiabatic Q_{acmb} is approximately 8.0 TW when taking the CMB temperature of $\sim\!4000~\rm K$ and adiabatic temperature gradient of $\sim\!1.0~\rm K\,km^{-1}$ (Labrosse, 2015) (see Table 1 and Supplementary Material Note-3). It is $\sim\!20\%$ less than the suggested heat flow across the core-mantle boundary (Q_{cmb} , $\sim\!10~\rm TW$). Our results show that the cooling rate of the Earth's core is most likely super-adiabatic ($Q_{cmb} > Q_{acmb}$); therefore, thermal convection can happen and contribute to the present-day geodynamo.

Venus as a near twin to Earth in size and mass, however, lacks a present-day magnetic field or continental-scale plate tectonics (Taylor et al., 2018). It remains an open question as to why Earth's

core supports a dynamo but the interior of Venus does not. Venus's stagnant lid likely reduces the cooling rate of its interior, which may imply a hotter core and lower CMB heat flow and makes dynamo action less likely (Driscoll and Bercovici, 2014). However, a low estimate of core thermal conductivity (20-40 W m⁻¹ K⁻¹) again raises the possibility of thermal convection in Venus's core. Although we still do not know the exact state and composition of the Venus's core, it is reasonable to assume an Fe-Ni-Si core and thus a similar thermal conductivity of \sim 52-73 W m $^{-1}$ K $^{-1}$. In this case, the cooling rate of the Venus's core must be sub-adiabatic, which would prevent a present-day dynamo if the inner core of Venus is also not growing fast enough to overcome the thermal stratification (Driscoll and Bercovici, 2014), or the core may be completely solid (O'Rourke et al., 2018).

4.2. Thermal conductivity in the outer and inner cores

The thermal conductivity (κ) decreases with radius (r) in the core, which can be assumed along the adiabat using a quadratic variation with radius (Labrosse, 2015):

$$\kappa\left(r\right) = \kappa_0 \left(1 - A_\kappa \frac{r^2}{L_\rho^2}\right) \tag{6}$$

$$\kappa (r) = \kappa_0 \left(1 - A_\kappa \frac{r^2}{L_\rho^2} \right)$$

$$L_\rho = \sqrt{\frac{3K_0}{2\pi G \rho_0^2}}$$

$$(6)$$

where κ_0 is the thermal conductivity at the Earth's center that varies with temperature and composition, which was taken from our modeled thermal conductivity of Fe-Ni-Si alloy, A_k is a constant of radial dependence of conductivity (2.39) (Gomi et al., 2013), ρ_0 is the density at the center of the core, G is the gravitational constant. Following Labrosse (2015), K_0 and L_ρ are estimated to be 1403 GPa and 8039 km for a 4-order polynomial least-squares fit of the density from PREM, respectively. The inner core is relatively depleted in light element(s) with respect to the outer core, making it more conductive; we, therefore, considered the light-element release effect on the thermal conductivity between the outer and inner core. The thermal conductivity for an Fe-5Ni-8Si outer core and an Fe-5Ni-4Si inner core can be modeled along the outer and inner core adiabat in Fig. 5a. The results show that the thermal conductivity jumps from ~ 101 to ~ 138 W m⁻¹ K⁻¹ across the inner-core boundary due to the exclusion of some light element Si from the inner core.

We compared the modeled electrical resistivities and thermal conductivities of Fe-Ni-Si alloys with the calculated results in liguid Fe-6.7Si (wt%) at the outer core conditions (de Koker et al., 2012) and solid hcp-Fe-4.2Si (wt%) at the inner core conditions (Pozzo et al., 2014) by first-principles molecular dynamics with the Kubo-Greenwood formula. Our modeled resistivities in Fe-Ni-Si are significantly higher than the calculations in liquid Fe-6.7Si (open diamonds, Fig. 4a), and the thermal conductivities in the core are systematically 40-50% lower than the calculated results (in Fig. 5a). The modeled thermal conductivity at the inner-core boundary is also considerably smaller than the recently calculated thermal conductivities of hcp-Fe-11Ni-5.3Si (inverted triangles in Fig. 5a) and hcp-Fe-11.3Ni-8.1Si alloys (triangles in Fig. 5a) at \sim 330 GPa and 5500 K by using the SPR-KKR-package (spin-polarized relativistic Korringa-Kohn-Rostoker) and the Kubo-Greenwood formula (Zidane et al., 2020). The possible reason is that the calculated resistivities and thermal conductivities of Fe-Si/Fe-Ni-Si alloys only considered electron-phonon scattering contribution to the transport properties, but recent work shows that the electron-electron scattering effect cannot be neglected in Fe and Fe alloys (Xu et al., 2018), especially at high temperatures. As a result, the previous calculations might overestimate the thermal conductivity, so more

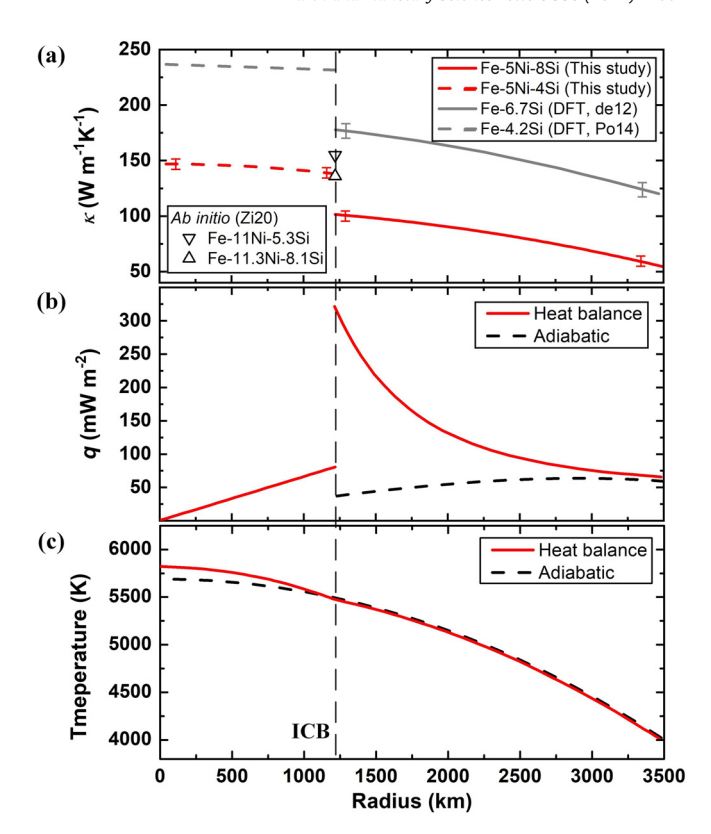


Fig. 5. Thermal conductivity (κ) , heat flux (q), and temperature profiles for Earth's core with Fe-Ni-Si alloy. (a) Modeled thermal conductivities of Fe-5Ni-4Si in the inner core and Fe-5Ni-8Si in the outer core, respectively. The outer and inner cores are modeled to be composed of ternary Fe-5Ni-8Si and Fe-5Ni-4Si alloys, respectively (Fischer et al., 2014; Mao et al., 2012; Zhang et al., 2018). The solid and dashed red lines represent modeled thermal conductivities of Fe-5Ni-8Si and Fe-5Ni-4Si at Earth's outer and inner core conditions, respectively. DFT calculations for the thermal conductivities of Fe-6.7Si liquid (de12) (de Koker et al., 2012) at the outer core conditions (solid gray line) and Fe-4.2Si alloy (Po14) (Pozzo et al., 2014) at the inner core conditions (gray dashed-line) are also plotted for comparisons. Open triangle and inverted triangle represent the calculated thermal conductivity of hcp-Fe-11Ni-5.3Si and hcp-Fe-11.3Ni-8.1Si at the ICB conditions (\sim 330 GPa and 5500 K) by ab initio method (Zidane et al., 2020). Calculated heat flux (b) and temperature profile (c) using modeled thermal conductivities in (a) and $Q_{cmb}=10.0$ TW. In the model, the total ICB heat flow Q_{icb} is \sim 6.0 TW, including the secular cooling of $Q_{qicb} = 1.5$ TW in this study, and the heat flow and gravitational energy of \sim 4.5 TW (Labrosse, 2015; Zhang et al., 2020). The heat flux densities and temperature profiles of the core are derived through heat balance (solid red lines) and adiabat (black dashed lines), respectively.

theory studies are needed to include the electron-electron scattering contributions. Based on our experimentally determined thermal conductivities at the topmost inner core (k_{tic}) , the adiabatic heat condition out of the inner core (Q_{aicb}) can be constrained to be \sim 1.5 TW (see Table 1 and Supplementary Material Note-3). The adiabatic Q_{aicb} contributes \sim 19% of the total adiabatic heat conduction out of the core (\sim 8.0 TW).

4.3. Heat flux and thermal structure of the core

We calculated the heat flux and thermal structure (temperature profile) of the core using the determined ICB temperatures, the thermal conductivity of the core, and the heat flow throughout the lowermost mantle (Q_{cmb}) . The temperature at the ICB is defined by the melting temperature for the outer core liquid, which is estimated to be around 5500 K for a core with $\sim\!8$ wt% Si according to the measured melting temperatures of Fe-Ni-Si alloys (Komabayashi et al., 2019; Zhang et al., 2018). The heat flux was then obtained from the heat balance of the core using a single volumetric model in Fig. 5b (see Supplementary Material Note-4). Considering the compositional energy of \sim 4.5 TW from latent heat and gravitational energy associated with the inner-core solidification for a CMB heat flow of $\sim\!10.0$ TW (Labrosse, 2015), the heat flux of the outer core shows a dramatic increase from $\sim\!65$ to $\sim\!321$ mW m $^{-2}$ towards the lowermost outer core. Compared with the adiabatic heat flux of $\sim\!38$ mW m $^{-2}$ at the lowermost outer core (dashed-line, Fig. 5b), the heat flux is approximately 8 times super-adiabatic due to the compositional energy. While the heat flux drops down to $\sim\!80$ mW m $^{-2}$ across the ICB.

We further estimated the temperature profiles of the outer and inner core through the heat balance (Fig. 5c) (see Supplementary Material Note-4). Taking the temperature of 5500 K at the ICB (Komabayashi et al., 2019; Zhang et al., 2018), the outer core temperature profile derived from the heat balance is consistent with an adiabatic profile that is ~4000 K at the CMB (Fig. 5c). While, the temperature of the core center derived from the heat balance is about 5820 K, and is approximately 120 K hotter than the adiabatic estimate (~5700 K). A super-adiabatic temperature profile in the inner core indicates that thermal convection in the inner core (Buffett, 2010). Inner core convection will not have an effect on the geodynamo, but it might contribute to lateral variations in heat flow and thus cause heterogeneity in seismic anisotropy observed at the top of the inner core (Buffett, 2010).

4.4. Sources of convection driving the geodynamo

The solid inner core is expected to form around \sim 1.5 Ga according to thermal evolution models of the core based on the determined heat flow across the CMB in this study (Gomi et al., 2013; Labrosse, 2015), significantly younger than the oldest paleomagnetic record of the Earth (\sim 3.45 Ga) (Tarduno et al., 2010). Therefore, sustaining the ancient geomagnetic field prior to inner core nucleation (ICN) requires a continual source of convection prior to the compositional source driven by inner core growth. The presence of core convection requires that the total core buoyancy flux (F_c) is positive. We calculated the total buoyancy flux containing thermal (F_T), conductive (F_a), and light element (F_χ) buoyancy fluxes (see Table 1 and Supplementary Material Note-5) (Driscoll and Bercovici, 2014),

$$F_c = F_T + F_{\gamma} - F_a \tag{8}$$

where the conductive buoyancy flux is subtracted because it represents thermal stratification and must be overcome to drive convection. For a heat flow Q_{cmb} of \sim 10.0 TW and a core thermal conductivity of \sim 50 W m⁻¹ K⁻¹ at present-day CMB, the buoyancy fluxes were calculated as a function of the CMB temperature from \sim 4300 to 3850 K in Fig. 6a. The CMB temperature gradually decreases with the cooling of the core, where for the early core, such as at \sim 3.0 Ga, it is estimated to be around 4300–4400 K (Labrosse, 2015). For simplicity, we assumed a constant CMB heat flux, so the thermal buoyancy flux is a constant value of \sim 1.4 \times 10⁻¹² m² s⁻³ (see Table 1 and Supplementary Material Note-5). This is likely an underestimate at higher T_{CMB} because a hotter core should cool faster

Our results show that the total buoyancy flux is positive, indicating the validity of a convective-driven geodynamo in this CMB temperature range in Fig. 6a. Specifically, the determined adiabatic heat flow satisfies the Schwarzschild's criterion for thermal convection over geological time (Schatten and Sofia, 1981). The total buoyancy flux gradually increased from $\sim 0.7 \times 10^{-13}$ to 1.5×10^{-13} m² s⁻³ with the cooling of the liquid core before inner-core nucleation, and the operation of the geodynamo depended entirely on thermal convection. At the onset of inner core growth (~ 1.5 Ga and ~ 4150 K at the CMB), the compositional buoyancy flux quickly increases. Within approximately 100

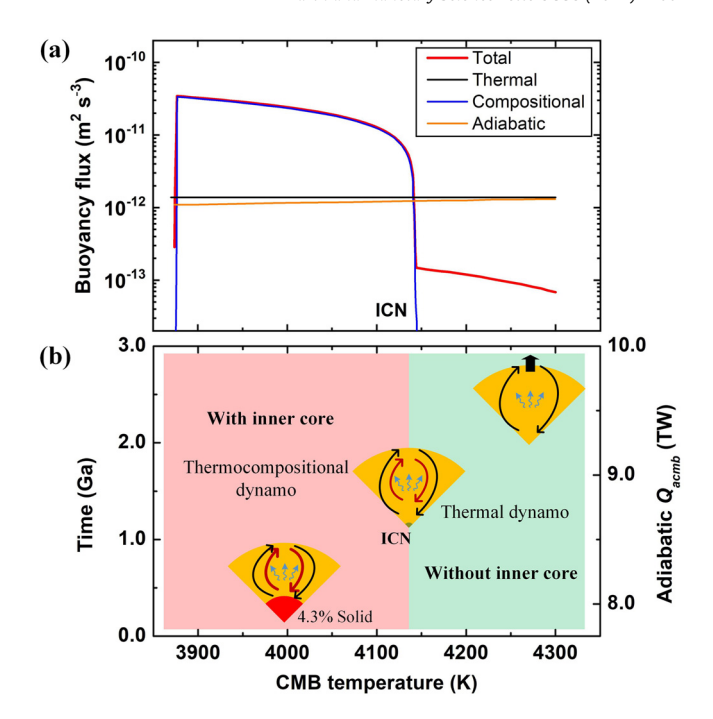


Fig. 6. Thermally versus compositionally-driven geodynamo over geological time. (a) Comparisons of thermal and compositional buoyancy fluxes in the core when taking CMB heat flow $Q_{cmb} = 10.0$ TW and present-day adiabatic heat flow $Q_{acmb} = 8.0$ TW. The core is fully liquid and thermally convective $(F_T > F_a)$ at the range of CMB temperature $T_{cmb} > \sim 4150$ K. Compositional convection occurs with the inner-core growth and drives the geodynamo together with thermal convection at the T_{cmb} between \sim 3850 and 4150 K. The present-day $T_{cmb} = \sim$ 4000 K and the core will be mostly solidified when T_{cmb} reaches below ${\sim}3850$ K. The melting temperature of the residual fluid at the CMB will drop over geological time as the inner core grows and releases light elements into the outer core. This leads to melting point suppression and thus additional cooling needed for the solidification of the residual core fluid, especially at the end of the inner core growth. (b) Evolution of adiabatic heat flow (Q_{acmb}) and geodynamo models with the cooling of the core over geological time. The geodynamo was mainly driven by thermal convection (black curved-arrow, thermal dynamo) with possible additional energy sources such as radiogenic heating (blue curved-arrow) or precipitation of chemical material out of the liquid core (Badro et al., 2016; O'Rourke and Stevenson, 2016) (black upward arrow) before ICN (\sim 1.5 Ga). After ICN, it has been driven by both thermally (black curved-arrow) and chemically compositional (red curved-arrow) convection and is named thermocompositional dynamo. Even though the present-day inner core accounts for only about 4.3 volume % of the whole core, it plays a significant role in the thermal evolution of the Earth. Orange and red areas represent the liquid and solid core, respectively.

million years after ICN with a T_{cmb} decrease of $\sim \! 10$ K (Driscoll and Bercovici, 2014), it rises to $\sim \! 10^{-12}$ m 2 s $^{-3}$, comparable with the thermal buoyancy flux ($\sim \! 1.4 \times 10^{-12}$ m 2 s $^{-3}$). As the inner core continuously grows the compositional buoyancy flux increases to above 2×10^{-11} m² s⁻³, which contributes above ~83% of the total buoyancy flux (\sim 2.4 × 10⁻¹¹ m² s⁻³) to power the presentday geodynamo. This implies that both thermal and compositional convection drive the present-day geodynamo and that compositional convection driven by the release of light elements at the ICB plays a dominant role (Fig. 6b). Our results show that the buoyancy flux of a thermal geodynamo is only about one-tenth of a thermocompositional geodynamo (Fig. 6a). It has been proposed that some additional energy sources, such as the precipitation of magnesium in the early liquid core (Badro et al., 2016; O'Rourke and Stevenson, 2016), might supplement the internal energy to power the early geodynamo before the inner-core formation. Additionally, the ohmic dissipation due to ohmic heating in the core could be another source to consider, but we should note that it is neglected in Equation (8). The magnitude of the ohmic dissipation remains largely uncertain (Nimmo, 2015), but could be as large as an adiabatic heat flow or above ~3 TW in one recent

study (Labrosse, 2015; Stelzer and Jackson, 2013). If the ohmic dissipation is substantial, the sum of the adiabatic heat flow of ~ 8 TW and the ohmic dissipation energy is required to power the geodynamo. In this scenario, even more power from compositional and/or radiative energy sources may be necessitated to sustain the geodynamo over geological time. Our results support thermal convection throughout the present outer core and do not support a thick thermal stratified layer at the top of the outer core based on the estimated convective flux (Takehiro and Sasaki, 2018). Nevertheless, we should note that a chemically stratified layer of $\sim 60-70$ km at the top of the outer core can possibly be formed because of the influx of oxygen from the lowermost mantle, perhaps through chemical interactions between an early magma ocean and the outer core (Brodholt and Badro, 2017), even if the heat flow is super-adiabatic.

5. Conclusions

The electrical resistivities of hcp Fe-10Ni and Fe-1.8Si alloys have been measured at the relevant P-T conditions of the Earth's core by a four-probe van der Pauw method coupled with in situ X-ray diffraction in laser-heated DACs. The temperature responses of the resistivities in hcp-Fe-1.8Si and Fe-10Ni alloys are guasilinear between \sim 1500 to 3400 K at high pressures of 80-140 GPa. Our results indicate that adding 1.8 wt% Si into hcp-Fe can significantly increase its resistivity by \sim 25% at \sim 140 GPa and 4000 K, but adding 10 wt% Ni into Fe only has a minor effect on its resistivity at near CMB P-T conditions. The thermal conductivity of Fe-5wt%Ni-8wt%Si as a candidate outer-core composition and Fe-5wt%Ni-4wt%Si as a candidate inner-core composition have been modeled based on the measured resistivities and the Wiedemann-Franz law. Consequently, the adiabatic heat flow out of the core is constrained to be \sim 8 TW. Our study implies that the thermal conductivity of an Fe-Ni-Si core is low enough to support a geodynamo driven by thermal convection over Earth's history. Additionally, both thermal and compositional convection drive the present-day geodynamo and the latter contributes predominantly.

CRediT authorship contribution statement

Y.Z. and J.F.L. designed the study. M.H. and Y.Z. prepared the cells, conducted resistivity measurements, and contributed equally in experiments. Y.Z., N.S., J.F.L., M.H., V.B.P., and E.G. conducted the synchrotron XRD experiments. Y.Z. analyzed the experimental data. P.D. performed the calculations of the heat flux and buoyancy flux. Y.Z., P.D., and J.F.L. wrote the paper. All the authors discussed the results and commented on the manuscript.

Declaration of competing interest

The authors declare that they have no actual or potential competing interests or personal relationships that could have influenced the work in this paper.

Acknowledgements

The authors thank Wenge Yang, Rossi Paul, and Qian Zhang for their assistance on the use of electrical resistivity system, and R.E. Cohen for discussions. We acknowledge Yanping Yang and Zhongli Fan for the FIB cutting, and William A. Basset and Leonid Dubrovinsky for sample syntheses. Youjun Zhang acknowledges financial support from the National Natural Science Foundation of China (41804082 and 42074098) and the Fundamental Research Funds for the Central Universities. Jung-Fu Lin acknowledges support from NSF Geophysics and CSEDI Programs (EAR-1901801 and EAR-1916941). High pressure-temperature resistivity experiments

were conducted at GeoSoilEnviroCARS of APS, ANL. We acknowledge the support of GeoSoilEnviroCARS (Sector 13), which is supported by the National Science Foundation-Earth Sciences (EAR-1634415), and the Department of Energy, Geosciences (DE-FG02-94ER14466). This research used resources of the Advanced Photon Source, a U.S. Department of Energy (DOE) Office of Science User Facility operated for the DOE Office of Science by Argonne National Laboratory under Contract No. DE-AC02-06CH11357. We thank Dr. James Badro, Dr. Joseph G. O'Rourke, and the anonymous reviewers who made constructive comments to significantly improve this manuscript.

Appendix A. Supplementary material

Supplementary material related to this article can be found online at https://doi.org/10.1016/j.epsl.2020.116614.

References

- Ammann, M.W., Walker, A.M., Stackhouse, S., Wookey, J., Forte, A.M., Brodholt, J.P., Dobson, D.P., 2014. Variation of thermal conductivity and heat flux at the Earth's core mantle boundary. Earth Planet. Sci. Lett. 390, 175–185.
- Asanuma, H., Ohtani, E., Sakai, T., Terasaki, H., Kamada, S., Hirao, N., Ohishi, Y., 2011. Static compression of Fe_{0.83}Ni_{0.09}Si_{0.08} alloy to 374 GPa and Fe_{0.93}Si_{0.07} alloy to 252 GPa: implications for the Earth's inner core. Earth Planet. Sci. Lett. 310, 113–118.
- Badro, J., Côté, A.S., Brodholt, J.P., 2014. A seismologically consistent compositional model of Earth's core, Proc. Natl. Acad. Sci. USA 111, 7542–7545.
- Badro, J., Brodholt, J.P., Piet, H., Siebert, J., Ryerson, F.J., 2015. Core formation and core composition from coupled geochemical and geophysical constraints. Proc. Natl. Acad. Sci. USA 112, 12310–12314.
- Badro, J., Siebert, J., Nimmo, F., 2016. An early geodynamo driven by exsolution of mantle components from Earth's core. Nature 536, 326–328.
- Boekelheide, Z., Cooke, D.W., Helgren, E., Hellman, F., 2009. Resonant impurity scattering and electron-phonon scattering in the electrical resistivity of Cr thin films. Phys. Rev. B 80, 134426.
- Brodholt, J., Badro, J., 2017. Composition of the low seismic velocity E' layer at the top of Earth's core. Geophys. Res. Lett. 44, 8303–8310.
- Buffett, B.A., 2010. Onset and orientation of convection in the inner core. Geophys. J. Int. 179, 711–719.
- de Koker, N., Steinle-Neumann, G., Vlček, V., 2012. Electrical resistivity and thermal conductivity of liquid Fe alloys at high P and T, and heat flux in Earth's core. Proc. Natl. Acad. Sci. USA 109, 4070–4073.
- Dewaele, A., Loubeyre, P., Occelli, F., Mezouar, M., Dorogokupets, P.I., Torrent, M., 2006. Quasihydrostatic equation of state of iron above 2 Mbar. Phys. Rev. Lett. 97, 215504.
- Dobson, D., 2016. Geophysics: Earth's core problem. Nature 534, 45.
- Driscoll, P., Bercovici, D., 2014. On the thermal and magnetic histories of Earth and Venus: influences of melting, radioactivity, and conductivity. Phys. Earth Planet. Inter. 236, 36–51.
- Driscoll, P.E., Du, Z., 2019. Geodynamo conductivity limits. Geophys. Res. Lett. 46, 7982–7989.
- Dziewonski, A.M., Anderson, D.L., 1981. Preliminary reference Earth model. Phys. Earth Planet. Inter. 25, 297–356.
- Fei, Y., Murphy, C., Shibazaki, Y., Shahar, A., Huang, H., 2016. Thermal equation of state of hcp-iron: constraint on the density deficit of Earth's solid inner core. Geophys. Res. Lett. 43, 6837–6843.
- Fischer, R.A., Campbell, A.J., Caracas, R., Reaman, D.M., Heinz, D.L., Dera, P., Prakapenka, V.B., 2014. Equations of state in the Fe–FeSi system at high pressures and temperatures. J. Geophys. Res., Solid Earth 119, 2810–2827.
- Gomi, H., Ohta, K., Hirose, K., Labrosse, S., Caracas, R., Verstraete, M.J., Hernlund, J.W., 2013. The high conductivity of iron and thermal evolution of the Earth's core. Phys. Earth Planet. Inter. 224, 88–103.
- Gomi, H., Hirose, K., Akai, H., Fei, Y., 2016. Electrical resistivity of substitutionally disordered hcp Fe–Si and Fe–Ni alloys: chemically-induced resistivity saturation in the Earth's core. Earth Planet. Sci. Lett. 451, 51–61.
- Hsieh, W.-P., Deschamps, F., Okuchi, T., Lin, J.-F., 2018. Effects of iron on the lattice thermal conductivity of Earth's deep mantle and implications for mantle dynamics. Proc. Natl. Acad. Sci. USA 115, 4099–4104.
- Hsieh, W.-P., Goncharov, A.F., Labrosse, S., Holtgrewe, N., Lobanov, S.S., Chuvashova, I., Deschamps, F., Lin, J.-F., 2020. Low thermal conductivity of iron-silicon alloys at Earth's core conditions with implications for the geodynamo. Nat. Commun. 11, 3332.
- Inoue, H., Suehiro, S., Ohta, K., Hirose, K., Ohishi, Y., 2020. Resistivity saturation of hcp Fe-Si alloys in an internally heated diamond anvil cell: a key to assessing the Earth's core conductivity. Earth Planet. Sci. Lett. 543, 116357.

- Komabayashi, T., Pesce, G., Sinmyo, R., Kawazoe, T., Breton, H., Shimoyama, Y., Glazyrin, K., Konôpková, Z., Mezouar, M., 2019. Phase relations in the system Fe-Ni-Si to 200 GPa and 3900 K and implications for Earth's core. Earth Planet. Sci. Lett. 512, 83–88.
- Konôpková, Z., McWilliams, R.S., Gómez-Pérez, N., Goncharov, A.F., 2016. Direct measurement of thermal conductivity in solid iron at planetary core conditions. Nature 534, 99–101.
- Labrosse, S., 2015. Thermal evolution of the core with a high thermal conductivity. Phys. Earth Planet, Inter. 247, 36–55.
- Li, J., Fei, Y., 2014. Experimental constraints on core composition. In: Turekian, K.K. (Ed.), Treat. Geochem., second edition. Elsevier, Oxford, pp. 527–557.
- Lin, J.-F., Heinz, D.L., Campbell, A.J., Devine, J.M., Mao, W.L., Shen, G., 2002. Ironnickel alloy in the Earth's core. Geophys. Res. Lett. 29, 1471.
- Lin, J.F., Scott, H.P., Fischer, R.A., Chang, Y.-Y., Kantor, I., Prakapenka, V.B., 2009. Phase relations of Fe-Si alloy in Earth's core. Geophys. Res. Lett. 36, L06306.
- Mao, Z., Lin, J.-F., Liu, J., Alatas, A., Gao, L., Zhao, J., Mao, H.-K., 2012. Sound velocities of Fe and Fe-Si alloy in the Earth's core. Proc. Natl. Acad. Sci. USA 109, 10239–10244.
- Matassov, G., 1977. The Electrical Conductivity of Iron-Silicon Alloys at High Pressures and the Earth's Core. University of California, Livermore, California, p. 180.
- Nimmo, F., 2015. Energetics of the core. In: Schubert, G. (Ed.), Treat. Geophys., second edition. Elsevier, Oxford, pp. 27–55.
- Ohta, K., Kuwayama, Y., Hirose, K., Shimizu, K., Ohishi, Y., 2016. Experimental determination of the electrical resistivity of iron at Earth's core conditions. Nature 534, 95-98.
- Olson, P., 2013. The new core paradox. Science 342, 431-432.
- O'Rourke, J.G., Stevenson, D.J., 2016. Powering Earth's dynamo with magnesium precipitation from the core. Nature 529, 387–389.
- O'Rourke, J.G., Gillmann, C., Tackley, P., 2018. Prospects for an ancient dynamo and modern crustal remanent magnetism on Venus. Earth Planet. Sci. Lett. 502, 46–56
- Pozzo, M., Alfè, D., 2016. Saturation of electrical resistivity of solid iron at Earth's core conditions. SpringerPlus 5, 256.
- Pozzo, M., Davies, C., Gubbins, D., Alfè, D., 2012. Thermal and electrical conductivity of iron at Earth's core conditions. Nature 485, 355–358.
- Pozzo, M., Davies, C., Gubbins, D., Alfè, D., 2014. Thermal and electrical conductivity of solid iron and iron-silicon mixtures at Earth's core conditions. Earth Planet. Sci. Lett. 393, 159–164.
- Schatten, K., Sofia, S., 1981. The Schwarzschild criterion for convection in the presence of a magnetic field. Astrophys. Lett. 21, 93–96.

- Siebert, J., Badro, J., Antonangeli, D., Ryerson, F.J., 2012. Metal-silicate partitioning of Ni and Co in a deep magma ocean. Earth Planet. Sci. Lett. 321–322, 189–197.
- Silber, R.E., Secco, R.A., Yong, W., Littleton, J.A., 2019. Heat flow in Earth's core from invariant electrical resistivity of Fe-Si on the melting boundary to 9 GPa: do light elements matter? I. Geophys. Res., Solid Earth 124, 5521–5543.
- Stacey, F.D., Loper, D.E., 2007. A revised estimate of the conductivity of iron alloy at high pressure and implications for the core energy balance. Phys. Earth Planet. Inter. 161, 13–18.
- Stelzer, Z., Jackson, A., 2013. Extracting scaling laws from numerical dynamo models. Geophys. J. Int. 193, 1265–1276.
- Takehiro, S.I., Sasaki, Y., 2018. On destruction of a thermally stable layer by compositional convection in the Earth's outer core. Front. Earth Sci. 6, 192.
- Tarduno, J.A., Cottrell, R.D., Watkeys, M.K., Hofmann, A., Doubrovine, P.V., Mamajek, E.E., Liu, D., Sibeck, D.G., Neukirch, L.P., Usui, Y., 2010. Geodynamo, solar wind, and magnetopause 3.4 to 3.45 billion years ago. Science 327, 1238–1240.
- Taylor, F.W., Svedhem, H., Head, J.W., 2018. Venus: the atmosphere, climate, surface, interior and near-space environment of an Earth-like planet. Space Sci. Rev. 214, 35.
- Volkov, B., 1984. Formation of local magnetic moments and resonant scattering in dilute chromium alloys containing nonmagnetic impurities. Sov. Phys., Solid State 26, 1471–1476.
- Williams, Q., 2018. The thermal conductivity of Earth's core: a key geophysical parameter's constraints and uncertainties. Annu, Rev. Earth Planet, Sci. 46, 47–66.
- Xu, J., Zhang, P., Haule, K., Minar, J., Wimmer, S., Ebert, H., Cohen, R., 2018. Thermal conductivity and electrical resistivity of solid iron at Earth's core conditions from first-principles. Phys. Rev. Lett. 121, 096601.
- Zhang, Y., Sekine, T., Lin, J.-F., He, H., Liu, F., Zhang, M., Sato, T., Zhu, W., Yu, Y., 2018. Shock compression and melting of an Fe-Ni-Si alloy: implications for the temperature profile of the Earth's core and the heat flux across the core-mantle boundary. J. Geophys. Res., Solid Earth 123, 1314–1327.
- Zhang, Y., Hou, M., Liu, G., Zhang, C., Prakapenka, V.B., Greenberg, E., Fei, Y., Cohen, R.E., Lin, J.-F., 2020. Reconciliation of experiments and theory on transport properties of iron and the geodynamo. Phys. Rev. Lett. 125, 078501.
- Zidane, M., Salmani, E.M., Majumdar, A., Ez-Zahraouy, H., Benyoussef, A., Ahuja, R., 2020. Electrical and thermal transport properties of Fe-Ni based ternary alloys in the Earth's inner core: an ab initio study. Phys. Earth Planet. Inter. 301, 106465.